This is a pre-print version of the paper. Please cite the final version of the paper:

D. A. G. Dell'Aglio, G. Di Martino, A. Iodice, D. Riccio, G. Ruello "A Unified Formulation of SAR Raw Signals From Extended Scenes for All Acquisition Modes With Application to Simulation", *IEEE Trans. Geosci. Remote Sens.*, vol. 56, no. 8, pp. 4956-4967, Aug. 2018. DOI: 10.1109/TGRS.2018.2844094.

IEEE Copyright notice. © 2018 IEEE. Personal use of this material is permitted. Permission from IEEE must be obtained for all other uses, in any current or future media, including reprinting/republishing this material for advertising or promotional purposes, creating new collective works, for resale or redistribution to servers or lists, or reuse of any copyrighted component of this work in other works.

This article has been accepted for inclusion in a future issue of this journal. Content is final as presented, with the exception of pagination.

A Unified Formulation of SAR Raw Signals From Extended Scenes for All Acquisition Modes With Application to Simulation

Domenico A. G. Dell'Aglio, *Student Member, IEEE*, Gerardo Di Martino, *Senior Member, IEEE*, Antonio Iodice, *Senior Member, IEEE*, Daniele Riccio, *Fellow, IEEE*, and Giuseppe Ruello, *Member, IEEE*

***Abstract*— Synthetic aperture radar (SAR) systems can generate microwave images by using different acquisition modes: stripmap, spotlight, scanSAR, and the more recently developed sliding spotlight and Terrain Observation by Progressive Scans (TOPSAR). The proper mode to be used is chosen according to the desired spatial resolution and coverage. In this paper, we present a unified formulation able to express raw signals of all acquisition modes. This formulation is then employed to show that both sliding spotlight and TOPSAR raw signal simulation of extended scenes can be achieved by using an improved version of the approach previously proposed by some of the authors for the sliding spotlight case. This approach implies a 1-D range Fourier-domain processing, followed by 1-D azimuth time-domain integration, and it can also precisely account for sensor trajectory deviations for any acquisition mode. Effectiveness of the proposed simulation scheme is assessed by using numerical examples. Results show that its computational load is much lower than the one of the time-domain approaches, and the obtained raw signals are in very good agreement with the exact ones. Finally, examples of simulations of SAR signals relative to extended, both canonical and realistic, scenes are also reported.**

***Index Terms*— Synthetic aperture radar (SAR), SAR simulation.**

I. Introduction

THE synthetic aperture radar (SAR) system can acquire data from a ground area under survey by using different operational modes. The standard, simplest one is the *stripmap* mode [1], [2]: the radar antenna is pointed along a fixed direction with respect to the platform flight path, and the antenna footprint covers a strip on the imaged surface as the platform moves. To improve the azimuth resolution by increasing the synthetic aperture length, at the expense of ground coverage, the *spotlight*, or *staring spotlight*, mode can be used [1], [2]: the radar antenna beam is steered during the overall acquisition time, pointing always at the same area over the ground. An intermediate solution is the so-called *hybrid stripmap/spotlight*, or *sliding spotlight*, mode [3]–[5]: the radar antenna beam is steered about a point farther away from the radar than the area being illuminated so that the antenna footprint on the ground moves more slowly than the sensor (it *slides*).

While staring and sliding spotlight modes aim at improving resolution at the expense of azimuth coverage, scanSAR [1], [2] and Terrain Observation by Progressive Scans (TOPSAR) [6] modes are aimed at improving range coverage (i.e., at extending the range swath) at the expense of azimuth resolution. In the scanSAR mode, a wide-range swath is obtained by periodically switching the antenna beam elevation to illuminate different range subswaths. Therefore, each subswath is periodically illuminated by *bursts* shorter than the stripmap integration time so that the azimuth resolution is worsened. To avoid the well-known annoying *scalloping* and space-varying ambiguity ratio effects of scanSAR images [1], [2], [6], the TOPSAR mode has been proposed: the antenna beam elevation is still periodically switched among different range subswaths, but within each burst, the beam is also steered from backward to forward (i.e., in the opposite way with respect to the staring or sliding spotlight cases) so that the antenna footprint on the ground moves faster than the sensor.

All above-described operational modes are today of great practical interest. In fact, while the first spaceborne SAR systems (such as European Remote Sensing Satellite and ENVISAT) employed stripmap and scanSAR modes, the most recent ones (namely, Cosmo/SkyMed, TerraSAR-X, and Sentinel-1) are also using sliding spotlight and/or TOPSAR modes. Accordingly, many different algorithms have been devised to process data acquired by using the different operational modes [1]–[10].

It is well-known that stripmap and staring spotlight modes can be considered as limiting cases of the sliding spotlight mode [4], and the TOPSAR has been conceived as a sliding spotlight with inverse beam rotation [6] so that similar approaches can be used to process data from both acquisition modes [7]–[10]. In addition, a unified raw signal formulation for all acquisition modes was proposed in [9] and [10] but

Manuscript received January 19, 2018; revised March 24, 2018 and May 22, 2018; accepted May 30, 2018. *(Corresponding author: Gerardo Di Martino.)*

The authors are with the Department of Electrical Engineering and Information Technology, University of Naples Federico II, 80125 Naples, Italy (e-mail: domenicoantoniogiuseppe.dellaglio@unina.it; gerardo.dimartino@unina.it; iodice@unina.it; daniele.riccio@unina.it; ruello@unina.it).

Color versions of one or more of the figures in this paper are available online at http://ieeexplore.ieee.org.

Digital Object Identifier 10.1109/TGRS.2018.2844094

0196-2892 © 2018 IEEE. Personal use is permitted, but republication/redistribution requires IEEE permission.
See http://www.ieee.org/publications_standards/publications/rights/index.html for more information.

This article has been accepted for inclusion in a future issue of this journal. Content is final as presented, with the exception of pagination.

only for a point target and only in space domain. However, at the best of our knowledge, a clear general, unified analytical formulation able to express raw signals acquired by all operational modes for extended scenes and both in space and frequency domains is not currently available in the literature. The first contribution of this paper is the presentation of such a unified formulation. By using the proposed raw signal formulation, we then show that both sliding spotlight and TOPSAR raw signal simulation of extended scenes can be achieved by using an improved version of the approach previously proposed by some of us for the sliding spotlight case [11], which implies a 1-D range Fourier-domain processing, followed by 1-D azimuth time-domain integration. This is the second contribution of this paper. It must be noted that the Fourier-domain approach allows exploiting the efficiency of fast Fourier transform (FFT) codes so that it is much more computationally convenient with respect to most of the wide literature on SAR simulation that is based on the time-domain approach (see [12], [13] for two recent examples). This is of fundamental importance when simulation of extended scenes has to be performed. In fact, in this case, all the operations needed to simulate the raw signal of a single-point target must be repeated for all the facets (smaller than system resolution), in which the scene surface must be subdivided, which usually are in the order of tens of millions. In addition, the scene reflectivity map must be evaluated based on the terrain topography and the scene's geometric and electromagnetic parameters. Note that [7]–[10] only deal with SAR focusing and do not present any SAR signal simulation scheme. Conversely, in [19], and [20], efficient TOPSAR simulation schemes were recently presented: they are both based on the proper azimuth filtering of wide-beam stripmap [20] or also spotlight [19] simulated raw signals. However, they both imply approximations whose range of validity is not demonstrated in [19] and [20] and cannot be analytically foreseen. Instead, our approach allows analytical evaluation of its validity range, as detailed in Appendix A. In addition, [19] and [20] only consider nominal, straight-line sensor trajectory at variance with our approach. In fact, as a third original contribution of this paper, the proposed simulation approach can also account for SAR sensor trajectory deviations for any acquisition mode (not only sliding spotlight and TOPSAR but also stripmap, scanSAR, and staring spotlight) more efficiently and precisely than what is currently available in the literature for Fourier-domain simulation approaches.

II. Unified Raw Signal Formulation

Let us consider an SAR sensor moving with velocity v along a straight line, coincident with the x-axis, and illuminating the ground with a steerable beam. Let us call X_1 the length of the trajectory flight portion used to acquire the raw data (or, for a scanSAR or TOPSAR system, the burst length) and r_0 the distance from the line of flight to the center of the imaged scene (see Fig. 1). If the beam is steered from forward to backward (as in the sliding spotlight case), its center of rotation is below the sensor, whereas if it is steered from backward to forward (as in the TOPSAR case), its center of

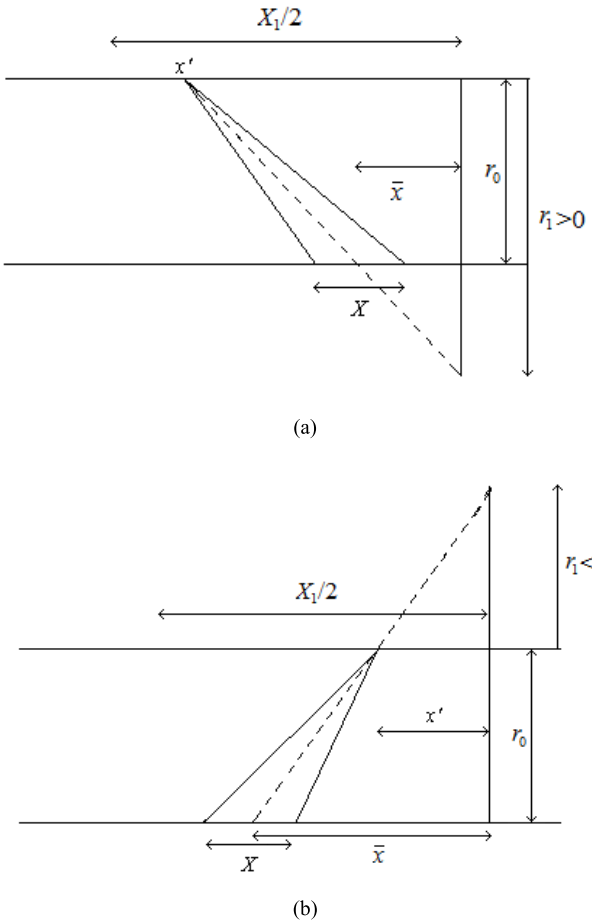

Fig. 1. (a) Sliding spotlight and (b) TOPSAR modes: illuminated area.

rotation is above the sensor. Let us call r_1 the *oriented distance* from the line of flight to the beam rotation center, assumed positive if the beam rotation center is below the sensor [see Fig. 1(a)] and negative if the beam rotation center is above the sensor [see Fig. 1(b)]. For the moment being, we will assume that no squint is present so that the trajectory flight center (that we take as the origin of the x-axis) is at the same abscissa as the scene center. In addition, for the sake of simplicity, we will also assume that $X_1 \ll |r_1|$, although the more general case could be considered as well. Let us now introduce the factor

$$A = \frac{r_1 - r_0}{r_1}. \tag{1}$$

It must be noticed that this factor is the same as the factor A defined in [4] for the sliding spotlight case and as the factor α introduced in [6] for the TOPSAR case, but here, it is defined in such a way that exactly the same formulation (1) can be used to express both: in this respect, it is very similar to the unified-model coefficient defined in [9] and [10]. By using simple geometrical considerations (see Fig. 1), it can be verified that the angular velocity of the antenna beam is

$$\omega_a = \frac{v}{r_1} = \frac{v}{r_0}(1 - A) \tag{2}$$

that the antenna azimuth footprint on the ground moves with velocity

$$v_f = Av \tag{3}$$

This article has been accepted for inclusion in a future issue of this journal. Content is final as presented, with the exception of pagination.

and that, when the sensor is at position x', the center of the antenna azimuth footprint is at

$$\bar{x} = Ax'. \tag{4}$$

Accordingly, the azimuth illumination diagram of the antenna is of the form

$$w\left(\frac{Ax' - x}{X}\right) \tag{5}$$

where $X = \lambda r_0 / L$ is the azimuth size of the antenna footprint [we assume that $w(\cdot)$ is negligible when the absolute value of its argument is larger than 1/2 and that it is an even function], L being the antenna azimuth length. Assuming a chirp modulation of the transmitted pulse, the expression of the SAR raw signal is then the following:

$$h(x', r') = \iint \gamma(x, r) g(x', r' - r; x, r) dx dr \tag{6}$$

where

$$\begin{aligned} & g(x', r' - r; x, r) \\ & = \exp\left[-j\frac{4\pi}{\lambda}\Delta R\right] \\ & \quad \times \exp\left[-j\frac{4\pi}{\lambda}\frac{\Delta f / f}{c\tau}(r' - r - \Delta R)^2\right] \\ & \quad \times \operatorname{rect}\left[\frac{(r' - r - \Delta R)}{c\tau/2}\right] w^2\left(\frac{Ax' - x}{X}\right) \operatorname{rect}\left[\frac{x'}{X_1}\right] \end{aligned} \tag{7}$$

is the SAR system impulse response, and

$$\Delta R = \Delta R(x' - x; r) = R - r = \sqrt{r^2 + (x' - x)^2} - r. \tag{8}$$

The following variables are used in (6)–(8) [see also Fig. 2 (with no deviations, i.e., $R_n \equiv R$)].

1) x, r, and θ are the coordinates in the cylindrical coordinate system whose axis is the sensor line of flight.
2) $S \equiv (x', 0, 0)$ is the sensor position.
3) r' is $c/2$ times the time elapsed from each pulse transmission.
4) $\gamma(x, r)$ is the scene reflectivity pattern,[1] including the phase factor $\exp[-j(4\pi/\lambda)r]$ and the range antenna pattern $w_r(r - r_0/S_r)$, S_r being the range size of the antenna footprint.
5) λ and f are the carrier wavelength and frequency of the transmitted signal, respectively.
6) R is the distance from S to the generic point $[x, r, \theta(x, r)]$ of the scene.
7) $\theta = \theta(x, r)$ is the soil surface equation.
8) Δf is the chirp bandwidth.
9) c is the speed of light.
10) τ is the pulse duration time.
11) rect$[\cdot]$ is the standard rectangular window function, i.e., rect$[\cdot] = 1$, if the absolute value of its argument is smaller than 1/2, otherwise rect$[\cdot] = 0$.

By analyzing the last two factors of (7) (or also by analyzing geometry in Fig. 1), we note that the synthetic antenna, with which a ground point at position x is observed, is made of trajectory points x' belonging at the same time to both the interval $[x/A - X/(2|A|), x/A + X/(2|A|)]$ and the interval $[-X_1/2, X_1/2]$. In addition, the fully focused ground area is made of the ground points x, such that the entire first interval, of size $X/|A|$, is included in the second one, of size X_1, if $X/|A| < X_1$, or the entire second interval is included in the first one if $X/|A| > X_1$. We can then realize that the synthetic antenna length of the fully focused ground points is

$$X_{SA} = \min\left\{\frac{X}{|A|},\ X_1\right\} \tag{9}$$

and that the azimuth size of the fully focused ground area is

$$X_F = ||A|X_1 - X|. \tag{10}$$

It must be noted that (2)–(10) hold for any real value of the factor A, and, by varying the latter, all acquisition modes can be obtained. In fact, for $A = 0$ (i.e., $r_1 = r_0$), the staring spotlight mode is obtained; for $0 < A < 1$ (i.e., $r_1 > r_0$), the above-mentioned expressions refer to the sliding spotlight mode; and $A = 1$ (i.e., $r_1 = \infty$) corresponds to the stripmap mode if $X_1 \gg X$ or to a burst of a scanSAR system if $X_1 < X$. For $A > 1$ (i.e., $r_1 < 0$), we get a burst of the TOPSAR mode, and (2) shows that the angular velocity of the antenna beam is in this case negative, coherently with the fact that the rotation is in the opposite direction with respect to the staring and sliding spotlight cases. Note that (2)–(10) also hold for

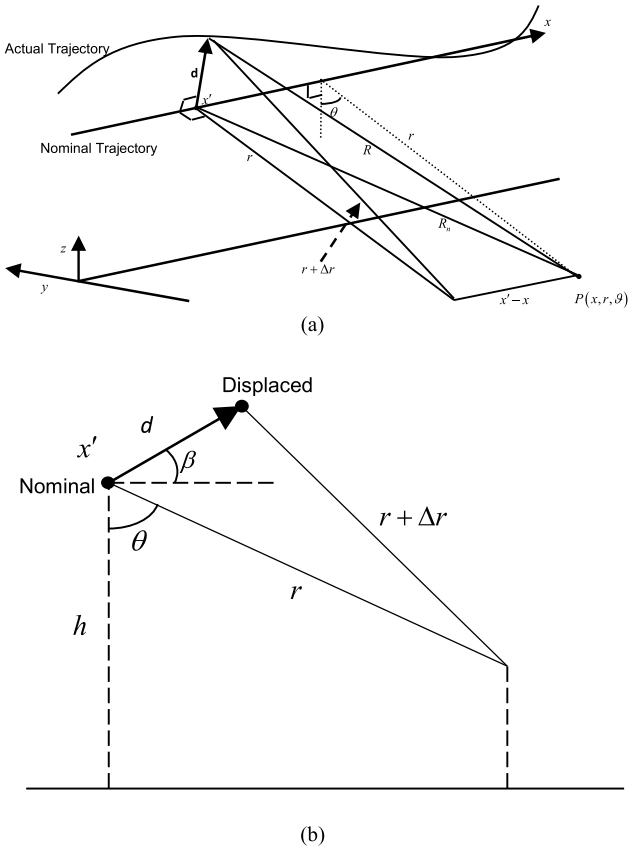

Fig. 2. Geometry of the problem, including possible trajectory deviations. (a) 3-D view. (b) 2-D lateral view.

[1]Hereafter, we will assume $\gamma(x', x, r) \approx \gamma(x, r)$. Actually, the reflectivity pattern of still ground point changes as the sensor moves, but the approximation is acceptable for the distances involved.

This article has been accepted for inclusion in a future issue of this journal. Content is final as presented, with the exception of pagination.

negative values of A, corresponding to $0 < r_1 < r_0$, i.e., to the case in which the beam rotation center is between the sensor and the ground. In this case, both the antenna beam rotation and the antenna ground footprint shift are from forward to backward ($\omega_a > 0$ and $v_f < 0$), and we get an *inverse* sliding spotlight mode if $-1 \leq A < 0$ and an *inverse* TOPSAR mode for $A < -1$. These inverse modes are less convenient than the direct ones, because the coverage and resolution properties are the same, but the antenna rotation velocity is higher. However, the inverse TOPSAR mode has been proposed in [14].

Additional useful information can be gained by expressing the raw signal in the 2-D Fourier transformed domain. In fact, a stationary phase evaluation of the FT of (6) and (7) along the same guideline of the stripmap and spotlight cases [2] leads to

$$H(\xi,\eta)=\iint \gamma(x,r)G(\xi,\eta;x,r)\exp[-j\xi x]\exp[-j\eta r]dxdr \tag{11}$$

where

$$\begin{aligned} &G(\xi,\eta;x,r)\\ &=\exp\left[j\frac{\eta^2}{4b}\right]\exp\left[j\frac{\xi^2(r/r_0)}{4a(1+\eta\lambda/(4\pi))}\right]\\ &\quad\cdot\operatorname{rect}\left[\frac{\eta}{bc\tau}\right]\operatorname{rect}\left[\frac{B(\xi-2ax)}{2aX}\right]w^2\left[\frac{A\xi-2a(A-1)x}{2aX}\right] \end{aligned} \tag{12}$$

is the SAR system transfer function (STF).

In (11) and (12), we have set

$$B=\frac{X}{X_1},\quad a=\frac{2\pi}{\lambda r_0},\ b=\frac{4\pi}{\lambda}\frac{\Delta f/f}{c\tau} \tag{13}$$

so that $B \ll 1$ for the stripmap mode, $B < 1$ for the staring and sliding spotlight modes, and $B > 1$ for the scanSAR mode; in addition, see the last three factors of (12), the range bandwidth is

$$\frac{\Delta\eta}{2\pi}=\frac{bc\tau}{2\pi}=\frac{2\Delta f}{c} \tag{14}$$

as it is well known, and the azimuth bandwidth of each fully focused ground point is

$$\frac{\Delta\xi}{2\pi}=\frac{a}{\pi}\min\left\{\frac{X}{|A|},X_1\right\}=\frac{2/L}{\max\{|A|,B\}}. \tag{15}$$

The overall azimuth bandwidth of the fully focused ground area can be obtained by analyzing the last two factors of (12) and using (10), and we get

$$\xi_{\max}-\xi_{\min}=\frac{2}{L}\left(1+\frac{X_1}{X}|1-A|\right)=\frac{2}{L}\left(1+\frac{|1-A|}{B}\right). \tag{16}$$

Finally, from (14) and (15), we straightforwardly get the SAR system slant range and azimuth resolutions

$$\rho_r=\frac{c}{2\Delta f},\quad \rho_a=\frac{L}{2}\max\{|A|,B\}. \tag{17}$$

Also (11)–(17) hold for any (positive, zero, or negative) real value of A, and they hold for any positive real value of B.

Finally, if a small squint angle ψ is present, (4) is replaced by $\bar{x}=Ax'+\psi r_0$ so that in the numerator of the argument of the azimuth illumination diagram w, a term ψr_0 must be added in (5) and (7) and a term $2a\psi r_0$ must be added in (12).

III. Simulation of SAR Raw Signals: Sliding Spotlight and TOPSAR Modes

In the stripmap, scanSAR, and staring spotlight cases, efficient simulation of raw signals relative to extended scene can be achieved by a full-2-D Fourier-domain approach [15], [16]. In fact, the x-dependence of the SAR STF in (12) is either absent (stripmap and scanSAR cases: $A = 1$) or it can be easily managed as explained in [16] (staring spotlight case: $A = 0$). In addition, the r-dependence of the SAR STF can be dominated by expanding the second exponential in (12), as illustrated in [2], [15], and [16]. Accordingly, the raw signal FT turns out to be equal to the (possibly *scaled*, see [2], [15], [16]) FT of the reflectivity multiplied by the SAR STF. Efficient 2-D FFT algorithms can be then exploited.

Conversely, in the general sliding spotlight and TOPSAR cases, while the r-dependence of the SAR STF can still be handled (see the following), no procedure can be implemented to manage its x-dependence and an efficient simulation algorithm cannot be devised in the 2-D Fourier domain. On the other hand, an algorithm in the space domain, directly based on (6)–(8), even if always possible, is not computationally efficient and, hence, not usable in practice if the extended scenes are considered. In [11], for the sliding spotlight case, we proposed an approach that involves 1-D range FTs. However, we there used a limited-range-swath assumption that is often reasonable for the sliding spotlight case but may be inappropriate for some TOPSAR systems. The method we propose here is still based on 1-D range FTs but it can relax the limited-range-swath assumption and can be employed for any acquisition mode.

Let us rewrite (6) and (7) as follows:

$$\begin{aligned} h(x',r')&=\operatorname{rect}\left[\frac{x'}{X_1}\right]\int dx\\ &\quad\times\left\{\int dr\,\gamma_1(x',x,r)g_1(x'-x,r'-r,r)\right\} \end{aligned} \tag{18}$$

where

$$\begin{aligned} &\gamma_1(x',x,r)\\ &=\gamma(x,r)\exp\left[-j\frac{4\pi}{\lambda}\Delta R(x'-x,r)\right]w^2\left[\frac{Ax'-x}{X}\right] \end{aligned} \tag{19}$$

$$\begin{aligned} &g_1(x'-x,r'-r,r)\\ &=\exp\left[-j\frac{4\pi}{\lambda}\frac{\Delta f/f}{c\tau}(r'-r-\Delta R)^2\right]\operatorname{rect}\left[\frac{r'-r-\Delta R}{c\tau/2}\right]. \end{aligned} \tag{20}$$

The 1-D range FT of $h(x',r')$ is

$$\begin{aligned} H_\eta(x',\eta)&=\int h(x',r')\exp(-j\eta r')dr'\\ &=\operatorname{rect}\left[\frac{x'}{X_1}\right]\int dx\\ &\quad\times\left\{\int dr\,\gamma_1(x',x,r)\exp(-j\eta r)\int dr'\right.\\ &\qquad\left.g_1(x'-x,r'-r,r)\exp[-j\eta(r'-r)]\right\}. \end{aligned} \tag{21}$$

This article has been accepted for inclusion in a future issue of this journal. Content is final as presented, with the exception of pagination.

The last integral in (21) can be readily evaluated by using the stationary phase method

$$\begin{aligned} G_1(x'-x,\eta,r) &= \int dr' g_1(x'-x,r'-r,r)\exp[-j\eta(r'-r)] \\ &= \exp\left[j\frac{\eta^2}{4b}\right]\mathrm{rect}\left[\frac{\eta}{bc\tau}\right]\exp(-j\eta\Delta R) \\ &= G_{10}(x'-x,\eta)\exp[-j\eta(\Delta R-\Delta R_0)] \end{aligned} \tag{22}$$

with

$$G_{10}(x'-x,\eta) = \exp\left[j\frac{\eta^2}{4b}\right]\mathrm{rect}\left[\frac{\eta}{bc\tau}\right]\exp(-j\eta\Delta R_0) \tag{23}$$

and

$$\Delta R_0 = \Delta R(x'-x, r=r_0) = \sqrt{r_0^2+(x'-x)^2} - r_0. \tag{24}$$

Now, if we assume $\eta(\Delta R - \Delta R_0) \ll 1$, which amounts to set a maximum limit to the range swath size (see Appendix A), then the last exponential in (22) is unitary so that we get

$$H_\eta(x',\eta) = \mathrm{rect}\left[\frac{x'}{X_1}\right]\int dx\, \Gamma_1(x',x,\eta) G_{10}(x'-x,\eta) \tag{25}$$

where $\Gamma_1(x',x,\eta)$ is the range-FT of $\gamma_1(x',x,r)$, and then, by an inverse FT

$$\begin{aligned} h(x',r') = \mathrm{rect}\left[\frac{x'}{X_1}\right]\int dx \\ \times\left\{\Im^{-1}\left[\Gamma_1\left(x',x,\eta\right)\cdot G_{10}(x'-x,\eta)\right]\right\}. \end{aligned} \tag{26}$$

We so obtain a simulation method similar to the one in [11]. Note that most part of the r-dependence of G is already accounted for in the exponential term of (19), and only the residual r-dependence of G_1 is neglected. Therefore, the assumption on range size is not extremely restrictive (see Appendix A) so that it can be safely made for sliding spotlight (see also [11]).

However, if above-mentioned assumption is not verified (as it may be the case in the TOPSAR case), we can still manage the r-dependence of G_1 by expanding ΔR around $r = r_0$, so obtaining

$$\Delta R - \Delta R_0 \cong \left(\frac{r_0}{\sqrt{r_0^2+(x'-x)^2}} - 1\right)(r-r_0). \tag{27}$$

Accordingly, we get

$$\begin{aligned} &H_\eta(x',\eta) \\ &= \mathrm{rect}\left[\frac{x'}{X_1}\right]\int dx\left\{\int d\bar{r}\gamma_1(x',x,\bar{r})\exp[-j\eta\Omega(x'-x)\bar{r}]\right. \\ &\qquad\left.\times G_{10}(x'-x,\eta)\right\} \\ &= \mathrm{rect}\left[\frac{x'}{X_1}\right]\int dx\Gamma_1[x',x,\eta\Omega(x'-x)]G_{10}(x'-x,\eta) \end{aligned} \tag{28}$$

where $\bar{r} = r - r_0$ and

$$\Omega(x'-x) = \frac{r_0}{\sqrt{r_0^2+(x'-x)^2}}. \tag{29}$$

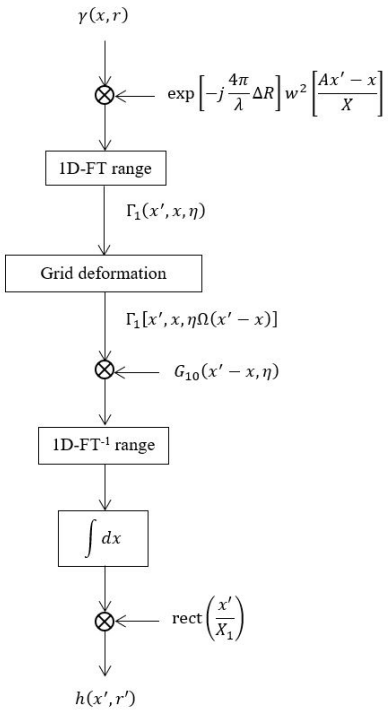

Fig. 3. Flowchart of SAR raw signal simulation. In the limited-range-swath case, the grid-deformation block can be removed.

We can finally write

$$\begin{aligned} h(x',r') = \mathrm{rect}\left[\frac{x'}{X_1}\right]\int dx \\ \times\left\{\Im^{-1}[\Gamma_1[x',x,\eta\Omega(x'-x)]\cdot G_{10}(x'-x,\eta)]\right\}. \end{aligned} \tag{30}$$

This expression suggests that the SAR raw signal simulation can be performed via the following steps (see Fig. 3).

1) *Generation of the Scene Reflectivity Pattern γ (x, r):* This step is performed exactly in the same way as described in [15]: the scene surface is subdivided in facets smaller than the final system resolution but much larger than wavelength. For each facet, the scattering coefficient is generated as a complex circular Gaussian random variable (characterized by the Rayleigh amplitude and uniform phase distribution) whose variance is computed according to the proper electromagnetic scattering model by considering incidence angle, polarization, and facet's roughness, conductivity, and permittivity (see [15] for details).
2) *For Each $x' \in [-X_1/2, X_1/2]$:* It has the following steps:
   a) Multiplication of $\gamma(x,r)$ by $\exp[-j(4\pi/\lambda)\Delta R]$ $w^2[(Ax'-x)/X]$ to obtain $\gamma_1(x',x,r)$.
   b) Implementation of 1-D FFT of $\gamma_1(x',x,r)$ to obtain $\Gamma_1(x',x,\eta)$.
   c) Interpolation in the η-Fourier domain to obtain the desired values $\Gamma_1(x',x,\eta\Omega(x'-x))$ from the available ones $\Gamma_1(x',x,\eta)$.
   d) Multiplication by $G_{10}(x'-x,\eta)$.

This article has been accepted for inclusion in a future issue of this journal. Content is final as presented, with the exception of pagination.

e) Implementation of 1-D inverse FFT to get $\Im^{-1}[\Gamma_1(x', x, \eta) \cdot G_{10}(x' - x, \eta)]$.
f) Integration over x.

This is the method employed in the simulator that we propose here for both the sliding spotlight modes and for each burst of the TOPSAR mode. Note that the interpolation in the η-Fourier domain can be efficiently performed by using grid deformation [15] or the chirp-scaling algorithm [2] so that the proposed method shows no substantial increase of computational complexity with respect to the method of [11]. Actually, the proposed method can be also applied for the stripmap, scanSAR, and staring spotlight modes, but in those cases, it is not convenient with respect to the methods of [15] and [16] which use a full-2-D Fourier-domain approach.

The presented procedure is certainly appropriate to spaceborne sensors: in fact, it assumes a straight-line flight path that is a good approximation for a few kilometres portion of the elliptical orbit of a satellite platform. Conversely, in the case of airborne sensors, appreciable deviations from the ideal trajectory may occur. Effects of these deviations can be easily accounted for by our simulation scheme since the azimuth processing is performed in time domain. Accordingly, it is sufficient to replace, in (19), (20), and (22), the expression (8) of ΔR with

$$\Delta R = \Delta R(x', x, r) = \sqrt{[r + \Delta r(x', x, r)]^2 + (x' - x)^2} - r \tag{31}$$

where $\Delta r(x', x, r)$ is the projection along the local line of sight of the deviation with respect to the nominal trajectory at the sensor azimuth location x'

$$\Delta r(x', x, r) = -d(x') \sin[\theta(x, r) - \beta(x')] \tag{32}$$

with $d(x')$ and $\beta(x')$ defining the platform displacement (see Fig. 2). In (32), it is assumed that $d \ll r_0$, which is always verified in practice.

Accordingly, (24), (27), and (29) are replaced, respectively, by

$$\Delta R_0 = \Delta R(r = r_0) = \sqrt{[r_0 + \Delta r(x', x, r_0)]^2 + (x' - x)^2} - r_0 \tag{33}$$

$$\Delta R - \Delta R_0 \cong \left(\frac{[r_0 + \Delta r(x', x, r_0)][1 + \Delta r'(x', x, r_0)]}{\sqrt{[r_0 + \Delta r(x', x, r_0)]^2 + (x' - x)^2}} - 1 \right) (r - r_0) \tag{34}$$

$$\Omega(x', x) = \frac{[r_0 + \Delta r(x', x, r_0)][1 + \Delta r'(x', x, r_0)]}{\sqrt{[r_0 + \Delta r(x', x, r_0)]^2 + (x' - x)^2}} \tag{35}$$

wherein (see Appendix B)

$$\Delta r'(x', x, r_0) = \left. \frac{\partial \Delta r}{\partial r} \right|_{r=r_0} \cong \frac{-d(x') \cos[\theta(x, r_0) - \beta(x')]}{r_0 \tan[\theta(x, r_0)]}. \tag{36}$$

Note that, again, no increase in the computational complexity is implied by this method of accounting for trajectory deviations. Also note that in [11], $\Delta r(x', x, r)$ was approximated by $\Delta r(x') = \Delta r(x', x, r_0)$, which is not necessary, as shown here. Finally, the method proposed here to account for trajectory deviations has a computational complexity similar to that of the method in [17], which, however, only applies to the stripmap mode. In addition, at variance with [17] and [18], no constraints on trajectory deviation amplitude are necessary (except that they are small compared to r_0, as it always happens in practice).

In conclusion, the proposed method can simulate raw signals with any acquisition mode, accounting for trajectory deviations. Accordingly, the very recent interesting method proposed in [21], able to obtain an SAR raw signal in case of trajectory deviations from several straight-trajectory simulated SAR raw signals, is not necessary with our approach. However, the method in [21], used in conjunction with our or other simulators, can be useful if one wants to efficiently simulate raw signals for several nonrectilinear sensor trajectories with the same nominal straight-line trajectory.

IV. Performance Evaluation

A. Computational Complexity

In order to evaluate the performance of the proposed simulation scheme, let us first compare its computational complexity with the one of a full time-domain direct approach. In this analysis, we do not consider the generation of the reflectivity map, which is the same in both approaches.

We call N_1 the number of pulses within a burst length X_1, N the number of scene pixels within one azimuth footprint X, N_r the number of range pixels within the slant range swath S_r, and N_τ the number of samples of the transmitted pulse of duration τ. It turns out that

$$N_1 = X_1 \frac{\text{PRF}}{v} = \frac{X \,\text{PRF}}{v} \cdot \frac{1}{B} \tag{37}$$

$$N = \frac{X \,\text{PRF}}{v} \cdot \frac{1}{\max\{|A|, B\}} \tag{38}$$

$$N_r = S_r \frac{2 f_s}{c} \tag{39}$$

$$N_\tau = \tau f_s \tag{40}$$

where PRF is the pulse repetition frequency and f_s is the sampling frequency.

If the raw signal is evaluated in time domain directly from (6)–(8), the efficiency of FFT codes is not exploited and the computational complexity (measured by the number of complex multiplications N_{TD}) is

$$N_{\text{TD}} \approx N_1 N \, N_\tau \, N_r. \tag{41}$$

As for the proposed 1-D Fourier-domain approach, computation of $\gamma_1(x', x, r)$ requires $N_1 N N_r$ complex multiplications, and its 1-D range FFT is calculated for each couple of values (x', x), so this step exhibits the computational complexity

$$N_1 N \frac{N_r}{2} \log_2 N_r. \tag{42}$$

This article has been accepted for inclusion in a future issue of this journal. Content is final as presented, with the exception of pagination.

TABLE I
MAIN SAR SYSTEM DATA USED IN THE SIMULATION RUNS

	Spaceborne	Airborne
Platform height (h)	693 km	6 km
Platform velocity (v)	7.5 km/s	0.142 km/s
Look angle (θ)	24 degrees	50 degrees
Azimuth antenna dimension (L)	12.0 m	0.9 m
Range antenna dimension	0.7 m	0.141 m
Carrier frequency (f)	5.405 GHz	5.31 GHz
Pulse duration (τ)	50 μs	7 μs
Pulse bandwidth (Δf)	50 MHz	37.5 MHz
Sampling frequency (f_s)	50 MHz	37.5 MHz
Pulse repetition frequency (PRF)	1642 Hz	329 Hz
A	2.9	2.9
B	0.5	0.5
Azimuth size of the scene	16.8 km	2.804 km
Ground range size of the scene	92.5 km	6.392 km
Azimuth resolution	17.4 m	1.302 m
Ground range resolution	7.4 m	5.221 m
Raw signal azimuth size	1537 pixels	2716 pixels
Raw signal range size	15040 pixels	1488 pixels

At this point, the matrix $\Gamma_1(x', x, \eta)$ is multiplied by the function $G(x' - x, \eta)$ for every value (x', x, η) and then the inverse 1-D range FFT of the updated matrix is evaluated. This stage exhibits the computational complexity

$$N_1 N\, N_r + N_1 N \frac{N_r}{2} \log_2 N_r. \tag{43}$$

Therefore, the overall computational complexity of the above-described algorithm (again measured by the number of complex multiplications $N_{1\mathrm{DFD}}$) is

$$N_{1\mathrm{DFD}} \approx N_1 N\, N_r (2 + \log_2 N_r). \tag{44}$$

Accordingly, by using the suggested 1-D Fourier-domain approach, processing time is reduced by the factor

$$\frac{N_{1\mathrm{DFD}}}{N_{\mathrm{TD}}} = \frac{2 + \log_2 N_r}{N_\tau} \tag{45}$$

with respect to a time-domain simulation. For instance, for $N_r = 8192$ and $N_\tau = 4096$, we obtain a processing time decrease factor of about 1/273. Note finally that if interpolation in the Fourier domain is needed (see Section III), the numerator of (45) only slightly increases (the exact amount depending on the employed interpolation technique) so that the very large advantage of the proposed simulation scheme with respect to the time domain is maintained.

B. Simulation Examples

We now move to test the accuracy of simulated raw signals. First of all, we want to verify that the raw signal corresponding to a single scattering point, simulated by using the proposed 1-D Fourier-domain approach, agrees with the one obtained directly from the exact time-domain expression, i.e., (6)–(8), where the reflectivity map $\gamma(\cdot)$ is a Dirac pulse so that no integration is needed.

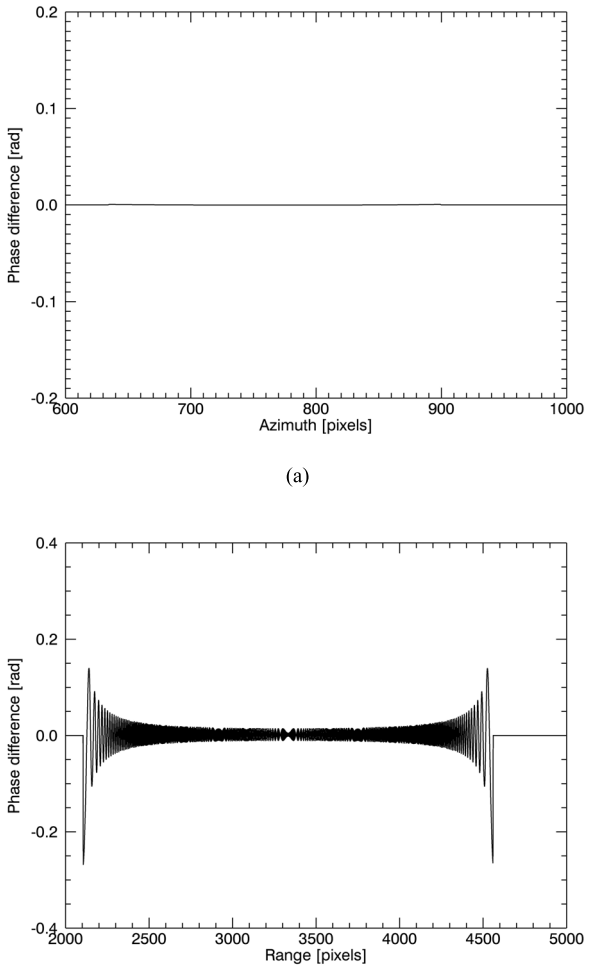

Fig. 4. (a) Azimuth and (b) range cuts of the phase difference between the raw signals simulated by using the proposed approach and the full time-domain simulation. Point scatterer placed at the scene center ($x = 0$, $r = r_0$).

We consider the system parameters similar to those of the Sentinel-1 spaceborne sensor, operating in the TOPSAR mode: they are reported in Table I (second column). We simulate the raw signal of a point scatterer placed at the center of the illuminated scene (i.e., the coordinates of the point scatterer are $x = 0$, $r = r_0$). First, phase error is considered, i.e., the phase difference between the raw signal simulated by using the proposed approach and the one obtained via full time-domain simulation: the results are shown in the plots of Fig. 4 with Fig. 4(a) reporting the cut of this phase difference along the azimuth direction and Fig. 4(b) the cut of the same phase difference along the range direction. It can be noted that the absolute value of this phase difference is always smaller, and often much smaller, than $\pi/10$, thus leading to negligible effects. Fast small oscillations in the range cut are due to

This article has been accepted for inclusion in a future issue of this journal. Content is final as presented, with the exception of pagination.

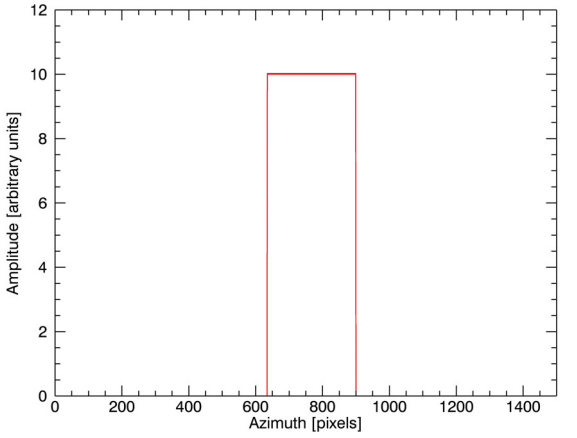

(a)

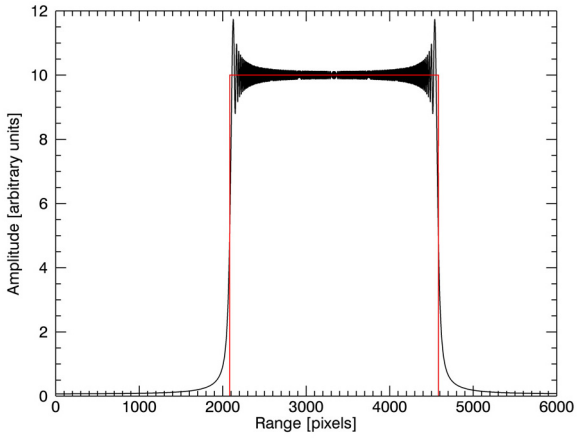

(b)

Fig. 5. (a) Azimuth and (b) range cuts of the amplitudes of the raw signals simulated by using the proposed approach (black line) and the full time-domain simulation (red line). Point scatterer placed at the scene center ($x = 0$, $r = r_0$).

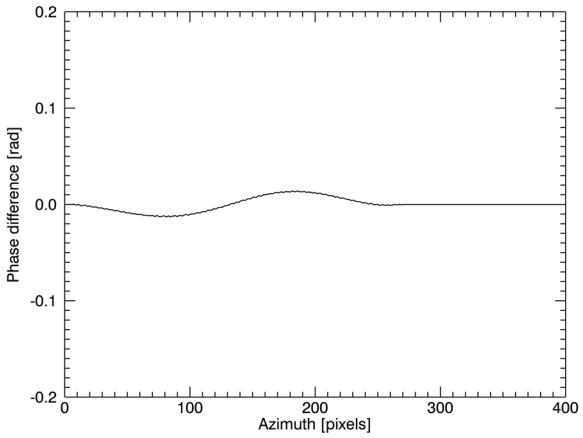

(a)

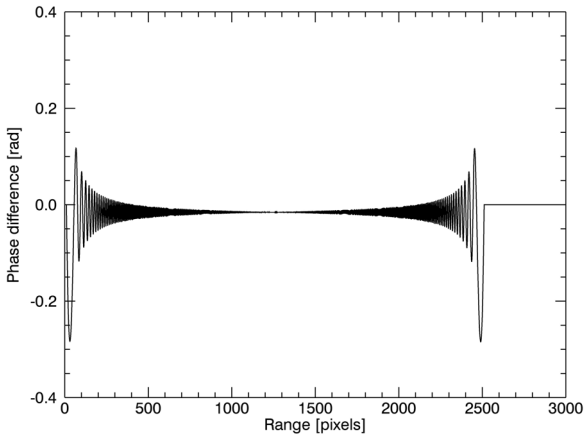

(b)

Fig. 6. (a) Azimuth and (b) range cuts of the phase difference between the raw signals simulated by using the proposed approach and the full time-domain simulation. Point scatterer placed at the near range scene border ($x = -8000$ m, $r = r_0 - 18\,300$ m).

the stationary phase method approximation and the Gibbs phenomenon.

Raw signal amplitudes are considered in Fig. 5, where azimuth and range cuts of the amplitudes of the raw signals obtained by the proposed approach and by using (6)–(8) are reported. Only small oscillations around the exact constant value can be noted in the range cut, again due to the stationary phase method approximation and to the Gibbs phenomenon, whereas the two azimuth cuts are almost perfectly overlapped and practically undistinguishable.

Similar comparisons for a point scatterer located at the azimuth and range borders of the illuminated area provide very similar results, as shown in Figs. 6 and 7: the only differences with respect to the previous case are very slight, negligible oscillations in the azimuth amplitude and phase cuts. Similar results are also obtained for different values of the system parameters.

A simulation relevant to an extended scene is now considered. We use the same spaceborne SAR system data of Table I (second column) and a "canonical" extended scene, constituted by a cone over a flat plane. In this experiment, we assume that outside the fully resolved area, the scene is perfectly absorbing. Corresponding raw signal has been generated. In Fig. 8, we show the image that can be obtained by using a TOPSAR focusing algorithm. As a final example of extended scene simulation of an actual scenario, we show in Fig. 9 the image obtained using the same system parameters of the previous simulation and providing as input to the simulator a digital elevation model of the southern Apennines area in Campania, Italy.

Finally, let us now consider an airborne sensor (see column 3 in Table I) with instable trajectory, operating in the TOPSAR mode. By using the approach described in Section III, we can deal with extended scenes and arbitrary trajectory deviations. However, for a simpler comparison, we here consider a scattering point located at the center of the illuminated scene and sinusoidal deviations with respect to the ideal trajectory. In particular, in our simulation, the trajectory sinusoidal deviation has a 1-m amplitude (when projected along the local line of sight) and a 157-m period.

This article has been accepted for inclusion in a future issue of this journal. Content is final as presented, with the exception of pagination.

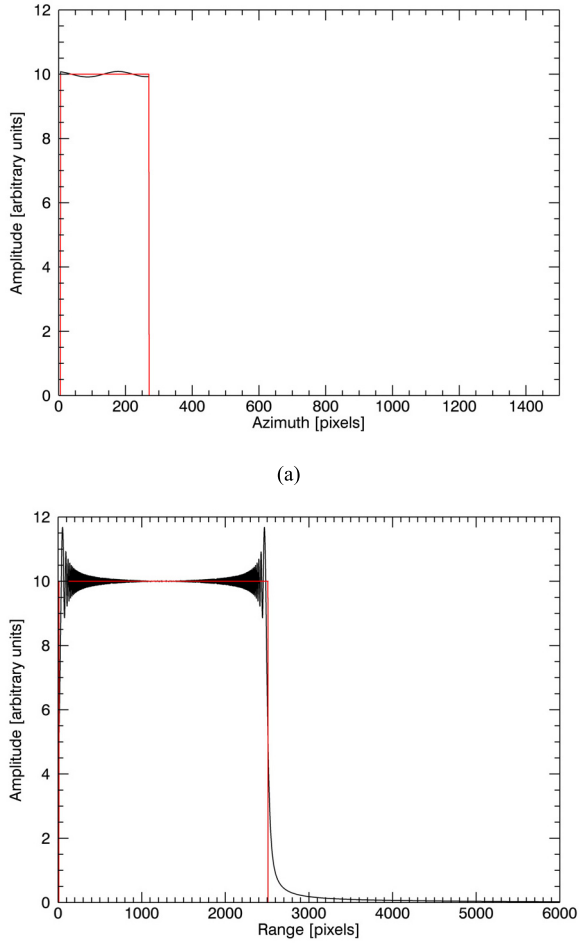

Fig. 7. (a) Azimuth and (b) range cuts of the amplitudes of the raw signals simulated by using the proposed approach (black line) and the full time-domain simulation (red line). Point scatterer placed at the near range scene border ($x = -8000$ m, $r = r_0 - 18\,300$ m).

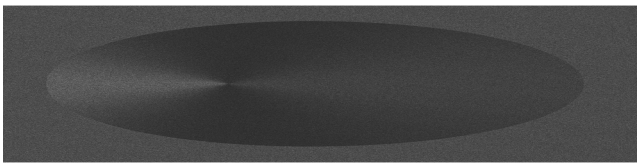

Fig. 8. Amplitude image obtained by focusing a simulated raw signal of a canonical extended scene constituted by a cone over a flat plane.

These are quite strong deviations. In Fig. 10, we show the azimuth and range cuts of the phase difference between the raw signal simulated by using the proposed approach and the one obtained via full time-domain simulation. Phase error is always smaller, and often much smaller, than $\pi/10$, thus confirming the validity of our approach. For the amplitudes, results similar to those of the spaceborne sensor with no trajectory deviations (see Figs. 5 and 7) are obtained.

A few last words are now needed about processing time. In the case of the simulation of the extended scene of Fig. 8, with a raw signal of 1537 (azimuth) $\times$ 15040 (range) samples, the raw signal simulation took about 40 min on a PC with an Intel Core 2 Duo Processor E8400 @ 3.00 GHz and 8-GB RAM. Note that time-domain processing of the same scene would require a processing time of the order of some days on the same PC.

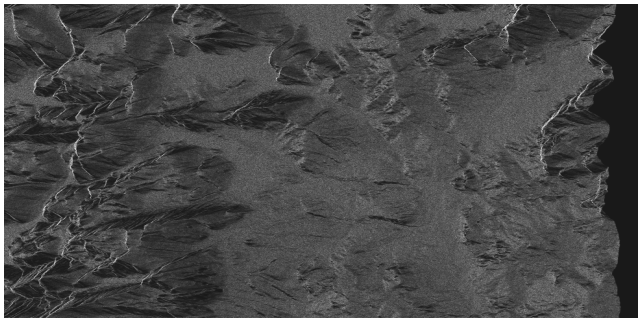

Fig. 9. Amplitude image obtained by focusing a simulated raw signal of the Apennines area in Campania, Italy. A multilook of two has been applied in the range direction to obtain an almost square pixel.

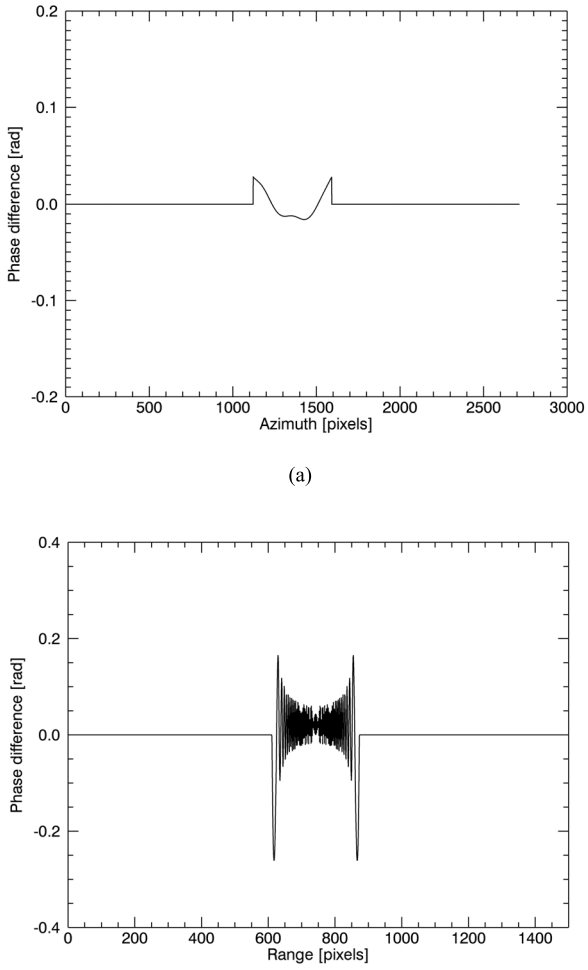

Fig. 10. (a) Azimuth and (b) range cuts of the phase difference between the raw signals simulated by using the proposed approach and the full time-domain simulation in the presence of sinusoidal trajectory deviations. Point scatterer placed at the scene center ($x = 0$, $r = r_0$).

V. Conclusion

In this paper, a unified analytical formulation of the SAR raw signals of extended scenes, expressed both in space and

This article has been accepted for inclusion in a future issue of this journal. Content is final as presented, with the exception of pagination.

in frequency domains and valid for all acquisition modes, has been presented. Based on this formulation, a simulation method has been proposed that allows to efficiently simulate SAR raw signals of extended scenes acquired with any acquisition mode, including the effects of trajectory deviations. It has been shown that this method is more accurate (since it makes less restrictive assumptions) and/or efficient than the available simulators for all acquisition modes, except for the cases in which a full 2-D Fourier-domain approach is possible, i.e., stripmap, scanSAR, and staring spotlight cases without trajectory deviations with respect to the ideal straight-line trajectory. In all other cases (i.e., sliding spotlight and TOPSAR modes with or without trajectory deviations, and stripmap, scanSAR, and staring spotlight cases with trajectory deviations), the proposed simulator is more accurate and/or efficient than existing ones. The proposed approach implies a 1-D range Fourier-domain processing, followed by 1-D azimuth time-domain integration. Computational complexity of the proposed simulation algorithm has been also analyzed, thus showing the enormous advantage with respect to the time-domain approach in terms of computing time. Finally, accuracy of the proposed simulation scheme has been assessed by comparing the raw signals that it generates with those generated by using the exact time-domain approach. Simulations of SAR signals relative to extended, both canonical and realistic, scenes have been also provided.

APPENDIX A

In this Appendix, we determine the conditions under which the approximation involved in (25) and (26) holds, i.e.,

$$\eta(\Delta R - \Delta R_0) \ll 1 \tag{46}$$

where ΔR_0 is given by (24).

The first factor in (46), i.e., η, is limited by the range bandwidth $bc\tau = (4\pi\Delta f/c)$. For the second

$$\begin{aligned}\Delta R - \Delta R_0 &\cong \frac{(x'-x)^2}{2r} - \frac{(x'-x)^2}{2r_0} = \frac{(x'-x)^2}{2r_0}\left(\frac{r_0}{r} - 1\right)\\ &\cong -\frac{(x'-x)^2}{2r_0^2}(r - r_0)\end{aligned} \tag{47}$$

where

$$|x' - x| \le \frac{|1-A|X_1 + X}{2} = \frac{X}{2}\left(1 + \frac{|1-A|}{B}\right) \tag{48}$$

and

$$|r - r_0| \le \frac{S_r}{2} \tag{49}$$

where S_r is the (slant) range extension of the imaged area. It follows that:

$$\Delta R - \Delta R_0 \le \frac{1}{8}\left(\frac{X}{r_0}\right)^2\left(1 + \frac{|1-A|}{B}\right)^2 \cdot \frac{S_r}{2}. \tag{50}$$

The final result is

$$\begin{aligned}&|\eta(\Delta R - \Delta R_0)|\\ &\le \frac{\pi\Delta f}{c}\frac{1}{2}\left(\frac{X}{r_0}\right)^2\left(1 + \frac{|1-A|}{B}\right)^2 \cdot \frac{S_r}{2}\\ &= \frac{2\pi 2\Delta f}{c}\left(\frac{\lambda 2}{L}\right)^2\left(1 + \frac{|1-A|}{B}\right)^2 \cdot \frac{S_r}{64} = \frac{2\pi}{\rho_r}\left(\frac{\lambda}{L/2}\right)^2\\ &\quad\times\left(1 + \frac{|1-A|}{B}\right)^2 \cdot \frac{S_r}{64}.\end{aligned} \tag{51}$$

Actually, for most of the values of the variables x, r, and η [over which integrations in (28)–(30) are performed], the phase term $\eta(\Delta R - \Delta R_0)$ is much smaller than the upper limit in (51) so that a sufficiently conservative condition to be set is

$$\frac{2\pi}{\rho_r}\left(\frac{\lambda}{L/2}\right)^2\left(1 + \frac{|1-A|}{B}\right)^2 \cdot \frac{S_r}{64} < \pi$$

i.e.,

$$S_r < \frac{32\rho_r\left(\frac{L/2}{\lambda}\right)^2}{\left(1 + \frac{|1-A|}{B}\right)^2}. \tag{52}$$

For instance, for a hypothetic high-resolution spaceborne sliding spotlight SAR system with $\lambda = 3$ cm, $L = 6$ m, $\rho_r = 1$ m, $B = 1/6$, and $A = 1/2$, we have $S_r < 20$ km. Approximately, the same result is obtained for a spaceborne TOPSAR system with $\lambda = 6$ cm, $L = 12$ m, $\rho_r = 3$ m, $B = 1/3$, and $A = 3$ (similar to the Sentinel-1 SAR system).

We finally note that our approximation in (27) amounts to neglect a term of the order of

$$\begin{aligned}\Delta R - \Delta R_0 - \left(\frac{r_0}{\sqrt{r_0^2 + (x'-x)^2}} - 1\right)(r - r_0)\\ \cong \frac{(x'-x)^2}{2r_0^3}(r - r_0)^2\end{aligned} \tag{53}$$

and the condition to be fulfilled in this case is

$$\frac{2\pi}{\rho_r}\left(\frac{\lambda}{L/2}\right)^2\left(1 + \frac{|1-A|}{B}\right)^2 \cdot \frac{S_r^2}{128 r_0} < \pi$$

i.e.,

$$S_r < \frac{8\sqrt{\rho_r r_0}\left(\frac{L/2}{\lambda}\right)}{\left(1 + \frac{|1-A|}{B}\right)}. \tag{54}$$

For instance, for the same hypothetic spaceborne sliding spotlight and TOPSAR systems as before, with $r_0 = 1000$ km, we get $S_r < 200$ km.

APPENDIX B

In this Appendix, we derive (34)–(36) from (31)–(33).

Expansion of (31) around r_0, arrested at the first order, gives

$$\begin{aligned}&\Delta R - \Delta R_0\\ &\cong \left.\frac{\partial\Delta R}{\partial r}\right|_{r=r_0}(r - r_0)\\ &= \left(\frac{[r_0 + \Delta r(x', x, r_0)]\left[1 + \left.\frac{\partial\Delta r(x', x, r)}{\partial r}\right|_{r=r_0}\right]}{\sqrt{[r_0 + \Delta r(x', x, r_0)]^2 + (x'-x)^2}} - 1\right)(r - r_0).\end{aligned} \tag{55}$$

This article has been accepted for inclusion in a future issue of this journal. Content is final as presented, with the exception of pagination.

Now, by using (32), we can write

$$\left.\frac{\partial \Delta r(x', x, r)}{\partial r}\right|_{r=r_0} = -d(x')\cos[\theta(x, r_0) - \beta(x')]\left.\frac{\partial \theta(x, r)}{\partial r}\right|_{r=r_0}. \quad (56)$$

Fig. 5(b) shows that

$$\theta(x, r) = \arccos\left(\frac{h - z(x, r)}{r}\right) \quad (57)$$

so that

$$\frac{\partial \theta(x, r)}{\partial r} = \frac{h - z(x, r) + r\frac{\partial z(x,r)}{\partial r}}{r^2 \sin[\theta(x, r)]} = \frac{1}{r\tan[\theta(x, r)]} + \frac{\frac{\partial z(x,r)}{\partial r}}{r\sin[\theta(x, r)]} \cong \frac{1}{r\tan[\theta(x, r)]} \quad (58)$$

where a moderate topography assumption is made to obtain the last approximate equality.

By replacing (58) in (56), we get

$$\left.\frac{\partial \Delta r(x', x, r)}{\partial r}\right|_{r=r_0} \cong -\frac{d(x')\cos[\theta(x, r_0) - \beta(x')]}{r_0\tan[\theta(x, r_0)]}$$

which is coincident with (36). Equation (35) is straightforwardly obtained from (55), i.e., from (34)

$$\Omega(x' - x) = 1 + \left.\frac{\partial \Delta R}{\partial r}\right|_{r=r_0} = \frac{[r_0 + \Delta r(x', x, r_0)][1 + \Delta r'(x', x, r_0)]}{\sqrt{[r_0 + \Delta r(x', x, r_0)]^2 + (x' - x)^2}}.$$

REFERENCES

[1] J. C. Curlander and R. N. McDonough, *Synthetic Aperture Radar: Systems and Signal Processing*. New York, NY, USA: Wiley, 1991.

[2] G. Franceschetti and R. Lanari, *Synthetic Aperture Radar Processing*. New York, NY, USA: CRC Press, 1999.

[3] D. P. Belcher and C. J. Baker, "High resolution processing of hybrid strip-map/spotlight mode SAR," *IEE Proc.-Radar, Sonar Navigat.*, vol. 143, no. 6, pp. 366–374, Dec. 1996.

[4] R. Lanari, S. Zoffoli, E. Sansosti, G. Fornaro, and F. Serafino, "New approach for hybrid strip-map/spotlight SAR data focusing," *IEE Proc.-Radar, Sonar Navigat.*, vol. 148, no. 6, pp. 363–372, Dec. 2001.

[5] J. Mittermayer, R. Lord, and E. Börner, "Sliding spotlight SAR processing for TerraSAR-X using a new formulation of the extended chirp scaling algorithm," in *Proc. IGARSS*, Toulouse, France, Jul. 2003, pp. 1462–1464.

[6] F. De Zan and A. M. Guarnieri, "TOPSAR: Terrain observation by progressive scans," *IEEE Trans. Geosci. Remote Sens.*, vol. 44, no. 9, pp. 2352–2360, Sep. 2006.

[7] P. Prats, R. Scheiber, J. Mittermayer, A. Meta, and A. Moreira, "Processing of sliding spotlight and TOPS SAR data using baseband azimuth scaling," *IEEE Trans. Geosci. Remote Sens.*, vol. 48, no. 2, pp. 770–780, Feb. 2010.

[8] G. Sun, M. Xing, Y. Wang, Y. Wu, Y. Wu, and Z. Bao, "Sliding spotlight and TOPS SAR data processing without subaperture," *IEEE Geosci. Remote Sens. Lett.*, vol. 8, no. 6, pp. 1036–1040, Nov. 2011.

[9] W. Yang, J. Chen, H. Zeng, J. Zhou, P. Wang, and C.-S. Li, "A novel three-step image formation scheme for unified focusing on spaceborne SAR data," *Prog. Electromagn. Res.*, vol. 137, pp. 621–642, 2013.

[10] W. Yang, J. Chen, W. Liu, P. Wang, and C. Li, "A modified three-step algorithm for TOPS and sliding spotlight SAR data processing," *IEEE Trans. Geosci. Remote Sens.*, vol. 55, no. 12, pp. 6910–6921, Dec. 2017.

[11] G. Franceschetti, R. Guida, A. Iodice, D. Riccio, and G. Ruello, "Efficient simulation of hybrid stripmap/spotlight SAR raw signals from extended scenes," *IEEE Trans. Geosci. Remote Sens.*, vol. 42, no. 11, pp. 2385–2396, Nov. 2004.

[12] F. Zhang, C. Hu, W. Li, W. Hu, and H.-C. Li, "Accelerating time-domain SAR raw data simulation for large areas using multi-GPUs," *IEEE J. Sel. Topics Appl. Earth Observ. Remote Sens.*, vol. 7, no. 9, pp. 3956–3966, Sep. 2014.

[13] K.-S. Chen, L. Tsang, K.-L. Chen, T. H. Liao, and J.-S. Lee, "Polarimetric simulations of SAR at L-band over bare soil using scattering matrices of random rough surfaces from numerical three-dimensional solutions of Maxwell equations," *IEEE Trans. Geosci. Remote Sens.*, vol. 52, no. 11, pp. 7048–7058, Nov. 2014.

[14] A. Meta, P. Prats, U. Steinbrecher, J. Mittermayer, and R. Scheiber, "TerraSAR-X TOPSAR and ScanSAR comparison," in *Proc. EUSAR*, Jun. 2008, pp. 1–4.

[15] G. Franceschetti, M. Migliaccio, D. Riccio, and G. Schirinzi, "SARAS: A SAR raw signal simulator," *IEEE Trans. Geosc. Remote Sens.*, vol. 30, no. 1, pp. 110–123, Jan. 1992.

[16] S. Cimmino, G. Franceschetti, A. Iodice, D. Riccio, and G. Ruello, "Efficient spotlight SAR raw signal simulation of extended scenes," *IEEE Trans. Geosci. Remote Sens.*, vol. 41, no. 10, pp. 2329–2337, Oct. 2003.

[17] G. Franceschetti, A. Iodice, S. Perna, and D. Riccio, "Efficient simulation of airborne SAR raw data of extended scenes," *IEEE Trans. Geosci. Remote Sens.*, vol. 44, no. 10, pp. 2851–2860, Oct. 2006.

[18] G. Franceschetti, A. Iodice, S. Perna, and D. Riccio, "SAR sensor trajectory deviations: Fourier domain formulation and extended scene simulation of raw signal," *IEEE Trans. Geosci. Remote Sens.*, vol. 44, no. 9, pp. 2323–2334, Sep. 2006.

[19] W. Xu, Y. Deng, F. Feng, Y. Liu, and G. Li, "TOPS mode raw data generation from wide-beam SAR imaging modes," *IEEE Geosci. Remote Sens. Lett.*, vol. 9, no. 4, pp. 720–724, Jul. 2012.

[20] Y. Liu, W. Wang, S. Dai, B. Rao, and G. Wang, "A unified multimode SAR raw signal simulation method based on acquisition mode mutation," *IEEE Geosci. Remote Sens. Lett.*, vol. 14, no. 8, pp. 1233–1237, Aug. 2017.

[21] Y. Liu, W. Wang, X. Pan, Z. Gu, and G. Wang, "Raw signal simulator for SAR with trajectory deviation based on spatial spectrum analysis," *IEEE Trans. Geosci. Remote Sens.*, vol. 55, no. 11, pp. 6651–6665, Nov. 2017.

Domenico A. G. Dell'Aglio (S'17) was born in Naples, Italy, in 1985. He received the master's degree in telecommunication engineering from the University of Naples Federico II, Naples, in 2016, where he is currently pursuing the Ph.D. degree with the Department of Electrical Engineering and Information Technology.

Since 2018, he has been cooperating with the Regional Competence Centre for Cultural Heritage, Ecology, and Economy, Benecon SCaRL, Caserta, Italy, under the aegis of Airborne Remote Sensing Campaign to Contrast the Cannabis in Albania Project, in partnership with the Italian Financial Policy. His research interests include active and passive remote sensing and image processing (both optical and synthetic aperture radar).

This article has been accepted for inclusion in a future issue of this journal. Content is final as presented, with the exception of pagination.

Gerardo Di Martino (S'06–M'09–SM'17) was born in Naples, Italy, in 1979. He received the Laurea degree *(cum laude)* in telecommunication engineering and the Ph.D. degree in electronic and telecommunication engineering from the University of Naples Federico II, Naples, in 2005 and 2009, respectively.

From 2009 to 2016, he was with the University of Naples Federico II, where he was involved in projects regarding applied electromagnetics and remote sensing topics. From 2014 to 2016, he was with the Italian National Consortium for Telecommunications, Parma, Italy, and the Centro Regionale Information Communication Technology, Naples. He is currently an Assistant Professor of electromagnetics with the Department of Electrical Engineering and Information Technology, University of Naples Federico II. His research interests include microwave remote sensing and electromagnetics, with a focus on electromagnetic scattering from natural surfaces and urban areas, synthetic aperture radar (SAR) signal processing and simulation, information retrieval from SAR data, and electromagnetic propagation in urban areas.

Antonio Iodice (S'97–M'00–SM'04) was born in Naples, Italy, in 1968. He received the Laurea degree *(cum laude)* in electronic engineering and the Ph.D. degree in electronic engineering and computer science from the University of Naples Federico II, Naples, in 1993 and 1999, respectively.

In 1995, he was with the Research Institute for Electromagnetism and Electronic Components, Italian National Council of Research, Naples. From 1999 to 2000, he was with Telespazio S.p.A., Rome, Italy. From 2000 to 2004, he was a Research Scientist with the Department of Electronic and Telecommunication Engineering, University of Naples Federico II, where he has been a Professor of electromagnetics with the Department of Electrical Engineering and Information Technology since 2005. He has been a principal investigator or a co-investigator for several projects funded by the European Union, the Italian Space Agency, the Italian Ministry of Education and Research, the Campania Regional Government, and private companies. He has authored or co-authored over 300 papers, over 80 among them are published in refereed journals. His research interests include the field of microwave remote sensing and electromagnetics: modeling of electromagnetic scattering from natural surfaces and urban areas, simulation and processing of synthetic aperture radar signals, and electromagnetic propagation in urban areas.

Dr. Iodice received the 2009 Sergei A. Schelkunoff Transactions Prize Paper Award from the IEEE Antennas and Propagation Society for the best paper published in 2008 on the IEEE TRANSACTIONS ON ANTENNAS AND PROPAGATION. He was recognized by the IEEE Geoscience and Remote Sensing Society as a 2015 Best Reviewer of the IEEE TRANSACTIONS ON GEOSCIENCE AND REMOTE SENSING. He is the Chair of the IEEE South Italy Geoscience and Remote Sensing Chapter.

Daniele Riccio (M'91–SM'99–F'14) was born in Naples, Italy. He received the Laurea degree *(cum laude)* in electronic engineering from the University of Naples Federico II, Naples, in 1989.

He was a Research Scientist with the Italian National Research Council, Institute for Research on Electromagnetics and Electronic Components, Naples, from 1989 to 1994, a Guest Scientist with the German Aerospace Center (DLR), Munich, Germany, from 1994 to 1995, a Lecturer to the Ph.D. program with the Universitat Politecnica de Catalunya, Barcelona, Spain, in 2006, and with the Czech Technical University, Prague, Czech Republic, in 2012. His career has been developed at the University of Naples Federico II, where he is currently a Full Professor of electromagnetic fields with the Department of Electrical Engineering and Information Technology. He is the Coordinator of the Ph.D. School in Information Technology and Electrical Engineering, University of Naples Federico II, where he is also a Representative with the Assembly of the National Inter-University Consortium for Telecommunications and the Scientific Board of the Italian Society of Electromagnetism. He is also a member of the Cassini Radar Science Team, Pasadena, CA, USA. He has authored three books, including *Scattering, Natural Surfaces, and Fractals* (2007), and over 400 scientific papers. His research interests include microwave remote sensing, electromagnetic scattering, synthetic aperture radar with an emphasis on sensor design, data simulation, and information retrieval, and also the application of fractal geometry to remote sensing.

Dr. Riccio was a recipient of the 2009 Sergei A. Schelkunoff Transactions Prize Paper Award for the best paper published in 2008 on the IEEE TRANSACTIONS ON ANTENNAS AND PROPAGATION. He serves as an associate editor for some journals on remote sensing.

Giuseppe Ruello (S'00–M'04) was born in Naples, Italy, in 1975. He received the Laurea degree *(cum laude)* in telecommunication engineering and the Ph.D. degree in information engineering from the University of Naples Federico II, Naples, in 1999 and 2003, respectively.

In 2002 and from 2004 to 2005, he was a Visiting Scientist with the Department of Signal Theory and Communications, Universitat Politecnica de Catalunya, Barcelona, Spain. He is currently a Research Scientist and an Aggregate Professor with the Department of Electrical and Information Technology Engineering, University of Naples Federico II. His research interests include synthetic aperture radar (SAR) remote sensing, modeling of electromagnetic scattering from natural surfaces, fractal models, SAR raw signal simulation, modeling of electromagnetic field propagation in urban environment, and remote sensing techniques for low-income semiarid regions.